J Appl Electrochem (2009) 39:1943–1948
DOI 10.1007/s10800-009-9903-5

ORIGINAL PAPER

Improved performances of mechanical-activated $LiMn_2O_4$/MWNTs cathode for aqueous rechargeable lithium batteries

Shengyao Chen · Changhuan Mi · Linghao Su · Bo Gao · Qingbin Fu · Xiaogang Zhang

Received: 20 December 2008 / Accepted: 14 April 2009 / Published online: 2 May 2009

Abstract $LiMn_2O_4$/multi-walled carbon nanotubes (MWNTs) composite was synthesized by mechanical activation reaction followed by a heat-treatment (500 °C). The $LiMn_2O_4$ and $LiMn_2O_4$/MWNTs as cathodes were investigated in 1 M Li_2SO_4 by cyclic voltammetry (CV), galvanostatic charge/discharge (GC), and electrochemical impedance spectroscopy (EIS). The $LiMn_2O_4$/MWNTs cathode delivered higher discharge capacity (117 mAh g^{-1}) than $LiMn_2O_4$ (84.6 mAh g^{-1}). Furthermore, the results from EIS showed that $LiMn_2O_4$/MWNTs had a faster kinetic process for lithium ion intercalation/de-intercalation than $LiMn_2O_4$. Besides, $LiMn_2O_4$/MWNTs had better cycling stability and rate capability than $LiMn_2O_4$, which was confirmed by GC testing. SEM images showed that a three-dimensional network structure was formed during the mechanical activation, giving a decrease of particle size.

Keywords $LiMn_2O_4$ · MWNTs · Mechanical activated · Rate capability

1 Introduction

Spinel $LiMn_2O_4$ has been explored as a promising cathode material for lithium-ion batteries due to its advantages such as low cost, abundant precursors, non-toxicity, and high compatibility with environment [1, 2]. However, its cycling stability and power density are still unsatisfied because of a large polarization at high rates, which can be attributed to the slow lithium ions diffusion in the solid active materials [3–6].

Generally, nanostructure materials are beneficial for the improvement of the cycling stability because their larger surface area of nanostructure makes the effective current density larger during the discharge process. Thus, a great number of nanostructure materials had been fabricated, such as nanoparticles ($Li_4Ti_5O_{12}$, $LiMn_2O_4$) [7, 8], nanowires (Co_3O_4, TiO_2–B) [9, 10], nanotubes ($LiMn_2O_4$, V_2O_5) [11, 12], hollow spheres (V_2O_5, $LiMn_2O_4$) [13, 14], and so on. Besides, various modification approaches had been applied in for this target. One of the approaches was substituting a small fraction of the manganese-ions with several divalent or trivalent metal ions in the 16d sites [15–17], the other one was surface coating layer by metal oxides to avoid Mn dissolution [18–20].

As is well known, the MWNTs can not only increase the electronic conductivity but also play an important role in improving the Li^+ diffusion during the electrochemical reaction [21–23]. In this study, we synthesized $LiMn_2O_4$/MWNTs composite via mechanical activation of MWNTs and $LiMn_2O_4$, leading to an increment of the electronic conductivity as well as a decrease of the particle size. The effective contact area between the electrode and the electrolyte was enlarged due to the decrease of the particle size, resulting in the improvement of the electrochemical utilization of $LiMn_2O_4$. The advantage of this method was that, only by ball-milling with MWNTs and a subsequent heat-treatment, large scale $LiMn_2O_4$ particles were reduced and a three-dimensional network structure was formed with $LiMn_2O_4$ particles entwined by the MWNTs. The electrochemical reversibility, cyclic stability, and rate capability of $LiMn_2O_4$/MWNTs composite were superior to $LiMn_2O_4$.

S. Chen · C. Mi · L. Su · B. Gao · Q. Fu · X. Zhang (✉)
College of Material Science and Engineering, Nanjing University of Aeronautics and Astronautics, Nanjing 210016, People's Republic of China
e-mail: azhangxg@163.com

2 Experimental

All chemicals used in our experiment were of analytical grade and obtained from Shanghai Chemical Reagent Co. Ltd. MWNTs (diameter, ca. 20–40 nm; length, ca. 5–15 μm) were purchased from Shenzhen Nanotech Port Co. Ltd. (Shenzhen, China) and purified by ultrasonic treatment in 6 M nitric acid for 0.5 h and then refluxing in 2.6 M HNO_3 for 24 h before use.

In the synthesis of $LiMn_2O_4$, 9.33 g of $MnCO_3$ and 1.5 g of Li_2CO_3 were ground to a homogeneous mixture in a planetary Fritsch Pulverisette-6 high-energy ball mill at 100 rpm (RPM) for 60 min, using agate balls and an agate jar. The mixed fine powder was heated at 500 °C for 6 h, and then calcined at 750 °C in air for 12 h with intermittent grinding [24]. In the preparation of $LiMn_2O_4$/MWNTs composite, as-obtained $LiMn_2O_4$, MWNTs (5 wt%) and N-methyl-2-pyrrolidone (NMP) were mixed and ball-milled for 10 h. After drying at 90 °C for 10 h, the powders were pelletized and further heated at 500 °C for 1 h in nitrogen atmosphere. After cooling to room temperature, the mixture was ball-milled again for 10 h. Finally, the mixture was dried at 90 °C for another 10 h.

Phase purity of $LiMn_2O_4$ and $LiMn_2O_4$/MWNTs was analyzed by X-ray diffraction (Bruker D8 advance, Germany) with Cu K_α radiation ($\lambda = 0.15418$ nm) using a 2θ step of 0.02°. The morphology and structural properties of $LiMn_2O_4$ and $LiMn_2O_4$/MWNTs composites were observed by a scanning electron microscopy (Quanta 200) operated at 20.0 kV. Nitrogen adsorption–desorption isotherms were tested by Micromeritics ASAP2020 instrument. Samples were out-gassed for 10 h under vacuum at 573 K before measurement. The specific surface area was calculated using the Brunauer–Emmet–Teller (BET) equation, using data in the P/P_0 region between 0.05 and 0.15 [25]. The Barret–Joyner–Halenda (BJH) method was applied to analyze the pore size distributions using the adsorption branch [26].

$LiMn_2O_4$ and $LiMn_2O_4$/MWNTs electrodes were prepared according to the following steps: the mixture containing 85 wt% active material, 10 wt% acetylene black, and 5 wt% polytetrafluoroethylene (PTFE) was well mixed and then pressed onto a nickel grid (1.2×10^7 Pa) that served as current collector (surface 1 cm^2). For the electrochemical test, the experiments were carried out with a three-electrode cell using a platinum and saturated calomel electrode (SCE) as counter and reference electrodes, respectively. The electrolyte was 1 M Li_2SO_4 solution. A CHI-660B electrochemical workstation instrument was employed for cyclic voltammetry (CV), electrochemical impedance spectra (EIS), and galvanostatic charge/discharge (GC) tests. Electrochemical impedance spectra were measured at the open circuit potentials of the electrodes, with frequencies varying from 0.01 to 100, 000 Hz with amplitudes of 0.005 V.

3 Results and discussion

3.1 XRD analysis of as-prepared $LiMn_2O_4$ and $LiMn_2O_4$/MWNTs

XRD patterns of $LiMn_2O_4$ and $LiMn_2O_4$/MWNTs were provided in Fig. 1. Both samples showed the same crystalline cubic spinel phase structure without any impurities in which Li^+ ions occupied the tetrahedral (8a) sites, Mn^{4+} ions resided at the octahedral (16d) sites and O^{2-} ions were located at 32e sites [27]. The results were in well agreement with the standard spectra (JCPDS: 89-0118), indicating that MWNTs did not change the crystal structure of pure $LiMn_2O_4$. There was no obvious carbon diffraction peaks in the profile of $LiMn_2O_4$/MWNTs composite due to the low content of MWNTs. The crystallite size (D) was calculated by the Scherrer's equation: $D = 0.9\lambda/\beta\cos\theta$, from the full-width-at-half-maximum β of four strong reflection peaks corresponding to [111], [311], [400], and [440] planes [28, 29], and the mean value of the crystallite sizes was 54 nm for $LiMn_2O_4$ and 23 nm for $LiMn_2O_4$/MWNTs, respectively. It suggested that the particle size of $LiMn_2O_4$ was decreased during the mechanical activation.

3.2 SEM analysis of as-obtained $LiMn_2O_4$ and $LiMn_2O_4$/MWNTs

The SEM images of $LiMn_2O_4$ and $LiMn_2O_4$/MWCNTs were shown in Fig. 2. Clearly to see, the particles sizes of $LiMn_2O_4$ and $LiMn_2O_4$/MWCNTs were distinct, and the former particle size (ca. 100 nm) was much smaller than the

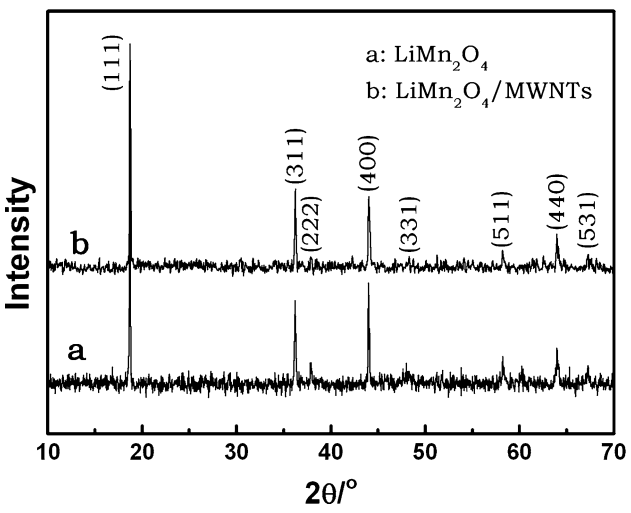

Fig. 1 XRD patterns for $LiMn_2O_4$ (**a**) and $LiMn_2O_4$/MWNTs (**b**)

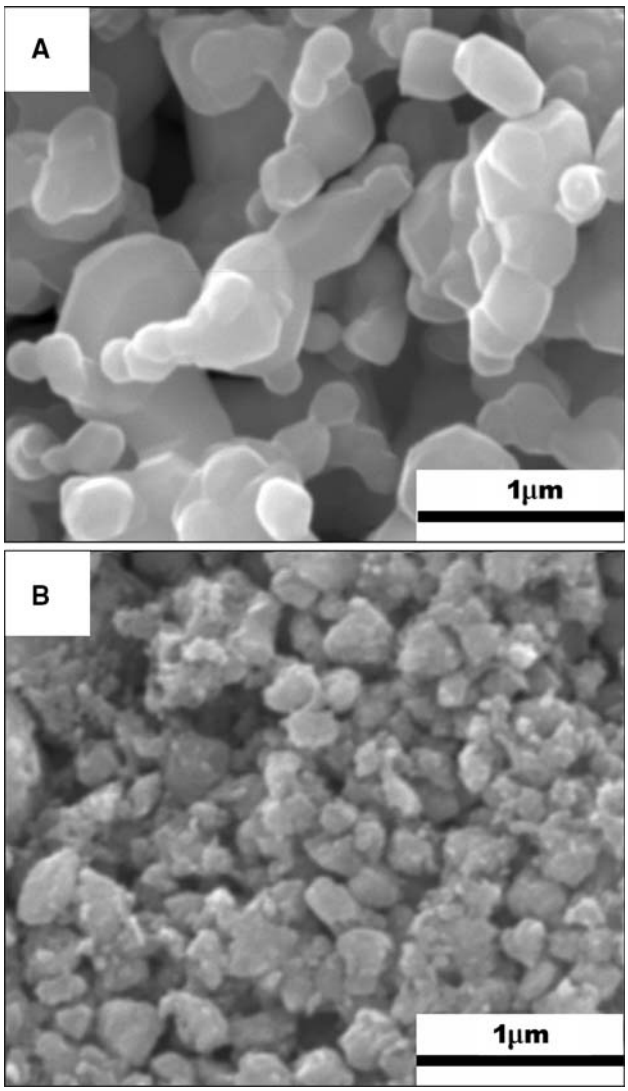

Fig. 2 SEM images of $LiMn_2O_4$ (**a**) and $LiMn_2O_4$/MWNTs (**b**)

latter one (ca. 500 nm). Since extremely fine (<1 nm) and extremely course (>20 μm) particle fractions were absent, the materials were suitable for electrode preparation techniques. In Fig. 2a, it was noted that the surface of $LiMn_2O_4$ particles was extremely smooth. In Fig. 2b, it could be observed that the MWNTs uniformly entwined $LiMn_2O_4$ particles after the ball-milling. The network structure contained the channels that allowed the electrolyte to penetrate into the electrode powder more freely. In other words, such morphology resulted in an increasing liquid/solid interfacial area and facilitated electrolyte diffusion. Therefore, this structure might be favorable for the insertion/extraction of Li^+ ions from the $LiMn_2O_4$ electrode. At the same time, the electronic conductivity was measured by a four-point probe method, 3.86×10^{-6} S cm^{-1} for $LiMn_2O_4$ and 1.08×10^{-1} S cm^{-1} for $LiMn_2O_4$/MWNTs. This result demonstrated that the MWNTs would provide extra pathways for electron transfer, which could improve the conductivity of the composite. Herein, the effects of mechanical ball-milling and MWNTs for the improved properties could be considered as a positive synergistic effect. $LiMn_2O_4$ particles entwined with the MWNTs by ball-milling. The electrochemical property improvement of the $LiMn_2O_4$/MWNTs composite could be attributed to the mechanical activation and the conductive agent MWNTs.

3.3 Nitrogen adsorption–desorption isotherms

Figure 3 showed nitrogen adsorption–desorption isotherms of $LiMn_2O_4$/MWNTs composite and the pore size distribution (PSD) curves (inset) obtained from the adsorption branches. The profile gave typical type-IV isotherms with a sharp inflection at relative pressure $P/P_0 > 0.4$, characteristic of capillary condensation, which indicated the uniformity of the mesopore size distribution. The PSD adsorption curve of $LiMn_2O_4$/MWNTs was centered at 25 nm. The BET specific surface area of $LiMn_2O_4$/MWNTs was 17.64 m^2 g^{-1}. These data confirmed the existence of the MWNTs, which could minimize the volume effect due to the large surface area during the charge/discharge process. The mesopores and macropores of $LiMn_2O_4$/MWNTs were very favorable for electrolyte penetration into the electrode [30, 31].

3.4 Electrochemical behaviors of $LiMn_2O_4$ and $LiMn_2O_4$/MWNTs

Figure 4 showed the CV curves of $LiMn_2O_4$ and $LiMn_2O_4$/MWNTs cathodes at a scan rate of 1 mV s^{-1}. For both $LiMn_2O_4$ and $LiMn_2O_4$/MWNTs, the CV curves included two redox couples, respectively. The electrochemical redox

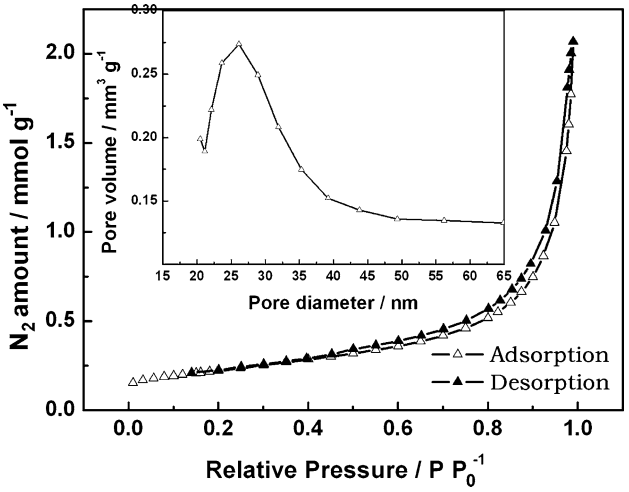

Fig. 3 Nitrogen adsorption-desorption isotherms and BJH pore size distribution plots (inset) of $LiMn_2O_4$/MWNTs composite

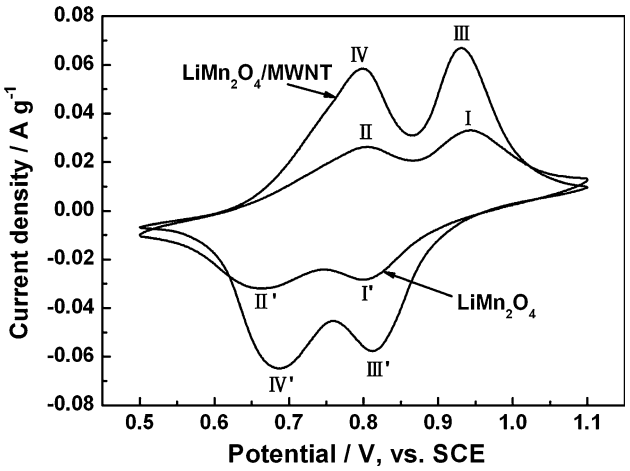

Fig. 4 The CV curves of $LiMn_2O_4$ and $LiMn_2O_4$/MWNTs at a scan rate of 1 mV s^{-1}

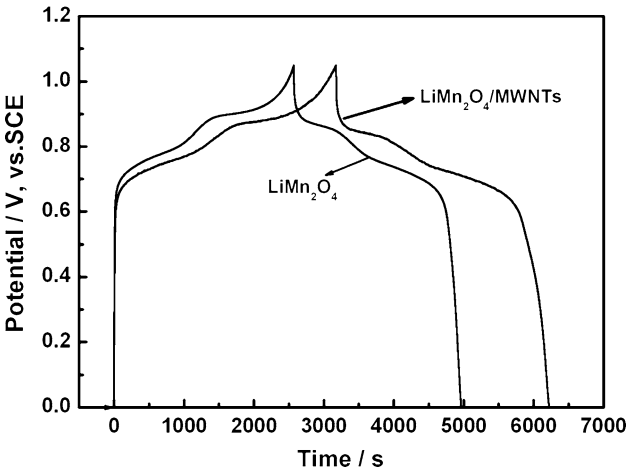

Fig. 5 The GC curves of $LiMn_2O_4$ and $LiMn_2O_4$/MWNTs for the first cycle at 0.1A g^{-1}

peaks of $LiMn_2O_4$/MWCNTs were more symmetric than those of $LiMn_2O_4$, indicating that the electrochemical reversibility of $LiMn_2O_4$/MWCNTs were superior to $LiMn_2O_4$ due to the improvement of the electronic conductivity. The electrochemical reversibility was evaluated by the potential differences between two redox peaks for $LiMn_2O_4$ and $LiMn_2O_4$/MWNTs composite (See Table 1). For $LiMn_2O_4$ electrode, two redox peaks differed with 0.146 V ($I - I'$) and 0.142 V ($II - II'$), respectively. However, for $LiMn_2O_4$/MWNTs electrode, the potential differences between two redox couples were 0.119 V ($III - III'$) and 0.111 V ($IV - IV'$), which were less than the potential differences of $LiMn_2O_4$. These results demonstrated the redox reactions in $LiMn_2O_4$/MWNTs electrode happened more easily, indicating that the cycling stability was improved. The possible reasons could be attributed to the decrement of the particle size, the enlarged contact areas and the enhanced electric conductivity due to MWNTs coating.

The GC curves of $LiMn_2O_4$ and $LiMn_2O_4$/MWNTs for the first cycle at 0.1 A g^{-1} were shown in Fig. 5. There were two charge/discharge plateaus corresponding to the $LiMn_2O_4$ and $LiMn_2O_4$/MWNTs, respectively. The $LiMn_2O_4$ electrode only delivered a capacity 84.6 mAh g^{-1}, whereas, the $LiMn_2O_4$/MWNTs delivered 117 mAh g^{-1} in 1 M Li_2SO_4 at 0.1 A g^{-1}. This result showed that the specific capacity of $LiMn_2O_4$ was improved by tethering with MWNTs coating on $LiMn_2O_4$ particles during the mechanical activation. The first redox plateau (about 0.9 V) was attributed to Li^+ ions removal from one-half of the tetrahedral sites, and the second redox plateau (about 0.75 V) was responded to the removal of Li^+ ions from the remaining tetrahedral sites. The two processes could be described as follows [32]:

$$LiMn_2O_4 \leftrightarrows Li_{0.5}Mn_2O_4 + 0.5Li^+ + 0.5e^- \quad (1)$$

$$Li_{0.5}Mn_2O_4 \leftrightarrows 2MnO_2 + 0.5Li^+ + 0.5e^- \quad (2)$$

The charge/discharge process represented by Eq. 1 took place at about 0.9 V with the cubic structure during this stage, while the second stage represented by Eq. 2 took place at about 0.75 V or lower with the crystal structure changing from cubic structure to tetragonal structure due to Jahn–Teller effect [32].

Figure 6 showed that (a) the cycling performance of $LiMn_2O_4$ and $LiMn_2O_4$/MWNTs at 0.1 A g^{-1} and (b) the discharge capacity of $LiMn_2O_4$ and $LiMn_2O_4$/MWNTs at various current densities in 1 M Li_2SO_4 solution. The discharge capacity of $LiMn_2O_4$ for the first cycle was 84.6 mAh g^{-1} at 0.1 A g^{-1}, and decreased to 50.1 mAh g^{-1} after 1,000 cycles. However, $LiMn_2O_4$/MWNTs cathode presented more stable discharge capacity retention than $LiMn_2O_4$, and the discharge capacity maintained 112.8 mAh g^{-1} until 1,000 cycles. The loss of specific capacity was only 3.59%. Figure 6b indicated the high rate capability of $LiMn_2O_4$/MWNTs electrode. When the current density reached 1.5 A g^{-1}, the capacity of $LiMn_2O_4$/MWNTs decreased to 87 mAh g^{-1}, but $LiMn_2O_4$ only delivered 18.2 mAh g^{-1}. The possible reasons for enhanced rate capabilities could be attributed to the enhanced electric conductivity as well as the decreased crystallite size during mechanical activation with MWNTs. The smaller particle size and larger surface area of $LiMn_2O_4$/MWNTs composite

Table 1 The potential differences between the oxidation peaks and reduction peaks for $LiMn_2O_4$ and $LiMn_2O_4$/MWNTs, respectively

$LiMn_2O_4$	I	I′	$I - I'$	II	II′	$II - II'$
E/V	0.943	0.797	0.146	0.806	0.664	0.142
$LiMn_2O_4$/MWNTs	III	III′	$III - III'$	IV	IV′	$IV - IV'$
E/V	0.931	0.812	0.119	0.798	0.687	0.111

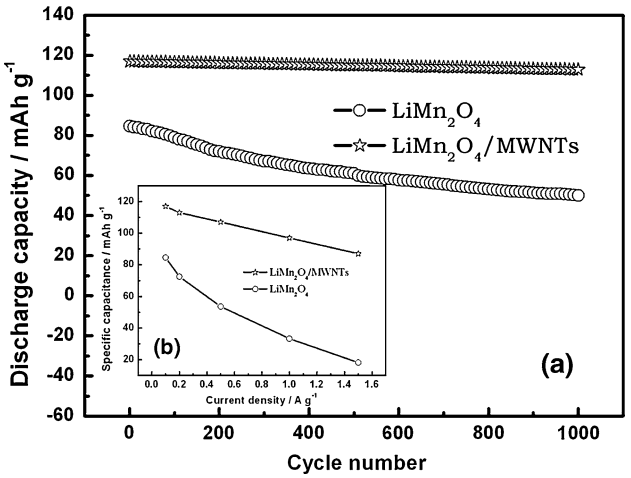

Fig. 6 **a** The cycling performance of $LiMn_2O_4$ and $LiMn_2O_4$/MWNTs at 0.1 A g^{-1}. **b** The discharge capacity of $LiMn_2O_4$ and $LiMn_2O_4$/MWCNTs at various current densities in 1 M Li_2SO_4 solution

might avoid the volume effect in the charge/discharge process. Therefore, the cycling stability and rate capability of $LiMn_2O_4$/MWNTs was superior to $LiMn_2O_4$.

3.5 Analysis of EIS spectra

Figure 7 presented the electrochemical impedance spectra of $LiMn_2O_4$ (*circle*) and $LiMn_2O_4$/MWNTs (*pentacle*), which were measured in fully discharged state after several cycles. The EIS spectra reflected the steps of the Li^+ insertion process, including the diffusion of Li^+ in solution, Li^+ migration through the surface film of $Li_xMn_2O_4$, charge-transfer for Li^+ intercalation, diffusion of Li^+ in the solid phase, and occupation of Li in the lattice [33, 34]. It is known that expansion and contraction of the particles occur during the charge/discharge process, and successive cycling leads to the increased electrical resistance within the cathode due to the passivation of the intercalation compound surface [35]. The fact that the MWNTs increased the conductivity of the electrode could also be derived from the impedance spectra. Levi et al. [36] suggested that the high–medium frequencies reflect Li migration through surface layers (the high-frequency semicircle) and medium-to-low frequency range reflects interfacial charge transfer (the medium semicircle). The high frequency semicircles in the EIS spectra of these electrodes were attributed to Li-ion migration through surface film that are formed on the Li_xMO_y cathode material (M = Co, Ni, Mn, etc.) [37].

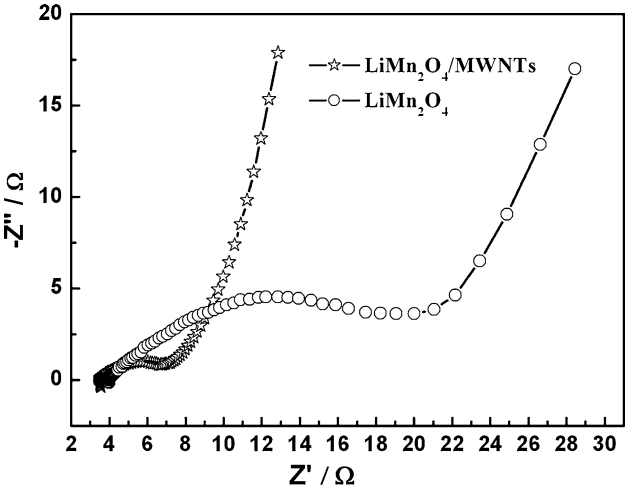

Fig. 7 The impedance spectra of $LiMn_2O_4$ (*circle*) and $LiMn_2O_4$/MWNTs (*pentacle*)

It could be seen from Fig. 7 that the charge-transfer resistance of $LiMn_2O_4$ was much larger than that of $LiMn_2O_4$/MWNTs. This indicated that the electrode reaction kinetics of $LiMn_2O_4$ was more sluggish than that of $LiMn_2O_4$/MWNTs. In addition, the value of charge transfer resistance (R_{ct}) for $LiMn_2O_4$ (18 Ω) was larger than that of $LiMn_2O_4$/MWNTs (4 Ω). This suggested that the electrode process of $LiMn_2O_4$/MWNTs had faster charge transfer kinetics. These results were consistent with the results in Figs. 4, 5 and 6.

4 Conclusion

$LiMn_2O_4$/MWNTs cathode was synthesized by mechanical ball-milling activation reaction followed by a heat treatment. The electronic conductivity of $LiMn_2O_4$/MWNTs with a three-dimensional network structure was measured to be 1.08×10^{-1} S cm^{-1}, which was five orders magnitude larger than that of $LiMn_2O_4$. Herein, the MWNTs increased the electronic conductivity and decreased crystallite size and the charge transfer resistance. Therefore, the cycling stability, rate capability, and reversibility of $LiMn_2O_4$/MWNTs were superior to $LiMn_2O_4$. These results suggested that the mechanical activation process could be used to improve the electrochemical performances of active materials by some modification means.

Acknowledgments This work was supported by National Basic Research Program of China (973 Program) (No.2007CB209700), National Natural Science Foundation of China (No.20633040, No. 20873064), and Graduate Innovation Plan of Nanjing University of Aeronautics and Astronautics (BCXJ08-08).

References

1. Park HS, Hwang SJ, Choy JH (2001) J Phys Chem B 105:4860
2. Kovacheva D, Gadjov H, Petrov K, Mandal S, Lazarraga MG, Pascual L, Amarilla JM, Rojas RM, Herrero P, Rojo JM (2002) J Mater Chem 12:1184

3. Yu LH, Yang HX, Ai XP, Cao YL (2005) J Phys Chem B 109:1148
4. Wang Y, Takahashi K, Shang HM, Cao GZ (2005) J Phys Chem B 109:3085
5. Jiao F, Shaju KM, Bruce PG (2005) Angew Chem Int Ed 44:6550
6. Arico AS, Bruce PG, Scrosati B, Tarascon JM, Schalkwijk V (2005) Nature Mater 4:366
7. Doi T, Iriyama Y, Abe T, Ogumi Z (2005) Chem Mater 17:1580
8. Curtis CJ, Wang JX, Schulz DL (2004) J Elctrochem Soc 151:A590
9. Nam KN, Kim DW, Yoo PJ, Chiang CY, Meethong N, Hammond P, Chiang YM, Belcher AM (2006) Science 312:885
10. Armstrong AR, Armstrong G, Canales J, Bruce PG (2004) Angew Chem Int Ed 43:2286
11. Li XX, Cheng FY, Guo B, Chen J (2005) J Phys Chem B 109:14017
12. Wang Y, Takahashi K, Lee KH, Cao GZ (2006) Adv Func Mater 16:1133
13. Cao AM, Hu JS, Liang HP, Wan LJ (2005) Angew Chem Int Ed 44:4391
14. Luo JY, Cheng L, Xia YY (2007) Electrochem Commun 9:1404
15. Yang ST, Jia JH, Ding L, Zhang MC (2003) Electrochimica Acta 48:569
16. Wagemaker M, Ooms FGB, Kelder EM, Schoolman J, Mulder FM (2004) J Am Chem Soc 126:13526
17. Alcantara R, Jaraba M, Lavela P, Tirado JL, Zhecheva E, Stoyanova R (2004) Chem Mater 16:1573
18. Eftekhari A (2004) Solid State Ion 167:237
19. Gnanaraj JS, Pol VG, Gedanken A, Aurbach D (2003) Electrochem Commun 5:940
20. Ha HW, Yun NJ, Kim K (2007) Electrochim Acta 52:3236
21. Li XL, Kang FY, Bai XD, Shen WC (2007) Electrochem Commun 9:663
22. Chen JJ, Whittingham MS (2006) Electrochem Commun 8:855
23. Sakamoto JS, Dunn B (2002) J Electrochem Soc 149:A26
24. Li XF, Xu YL (2007) Electrochem Commun 9:2023
25. Brunauer S, Emmett PH, Teller E (1938) J Am Chem Soc 60:309
26. Barrett EP, Joyner LG, Halenda PP (1951) J Am Chem Soc 73:373
27. Thackeray MM, Johnson PJ, de Picciotto LA (1984) Mater Res Bull 19:179
28. Sanchez MAE, Brito GES, Fantini MCA, Goya GF, Matos JR (2006) Solid State Ion 177:497
29. Abe T, Mizutani Y, Tabuchi T, Ikeda K, Asano M, Harada T, Inaba M, Ogumi Z (1997) J Power Sources 68:216
30. Hu CC, Chang KH, Lin MC, Wu YT (2006) Nano Lett 6:2690
31. Wang DW, Li F, Liu M, Lu GQ, Cheng HM (2008) Angew Chem Int Ed 47:373
32. Armand M, Dalard F, Reroo D, Mouliom C (1985) Solid State Ion 15:205
33. Bisquert J, Belmonte GG, Bueno P, Longo E, Bulhoes LOS (1998) J Electroanal Chem 452:229
34. Lu DS, Li WS, Zuo XX, Yuan ZZ, Huang QM (2007) J Phys Chem C 111:12067
35. Su LH, Zhang XG, Liu Y (2008) J Solid State Electrochem 12:1129
36. Levi MD, Gamolsky K, Aurbach D, Heider U, Oesten R (2000) Electrochim Acta 45:1781
37. Aurbach D, Markovsky B, Levi MD, Levi E, Schechter A, Moshkovich M, Cohen Y (1999) J Power Sources 81/82:95